Astrophys Space Sci (2020) 365:100
https://doi.org/10.1007/s10509-020-03819-0

ORIGINAL ARTICLE

An artificial neural network model of electron fluxes in the Earth's central plasma sheet: a THEMIS survey

Zhengyang Zou[1] · Yuri Y. Shprits[2,3] · Binbin Ni[4] · Nikita A. Aseev[2,3] · Pingbing Zuo[1] · Fengsi Wei[1]

Received: 14 January 2020 / Accepted: 8 June 2020

Abstract The Earth's central plasma sheet plays an important role in mass and energy transport in the whole magnetosphere. Here, we first present a new approach, i.e., an Artificial Neural Network (ANN) model, to investigate the electron number fluxes in the central plasma sheet. With the time series of 8 solar wind/geomagnetic indices and spatial locations as inputs, the model has been trained, validated, and tested with three isolated groups of measurements from Time History of Events and Macroscale Interaction during the Substorm (THEMIS) – A/D/E spacecraft from April 1, 2007 to December 30, 2015. The plasma sheet electron flux is shown to be accurately reproduced by the ANN model with a total correlation coefficient (R) above ∼0.91 and a root-mean-square-error (RMSE) less than 0.36 between the data and model target in a spatial region from radial distance 7 R_E to 12 R_E (where R_E is the Earth's radius) at the nightside of between 18 MLT through 24 MLT and up to 0.6 MLT (Magnetic Local Time) for energies at 0.06 – 293 keV. Global and spectral distributions of reproduced values can also capture the dawn-dusk asymmetry and the dependence on radial distances of plasma sheet electron fluxes. Our developed artificial neural network (ANN) therefore has a good capability in statistically reproducing the plasma sheet electron fluxes for a variety of substorm activities, and can be readily adopted for building up the boundary conditions for physics-based simulation efforts that model the dynamics of the radiation belt electrons and other parts of the terrestrial magnetosphere.

Keywords Plasma sheet electron number fluxes · Artificial Neural Network model · Global distributions · Energy spectrum

1 Introduction

The plasma sheet is located near the equator of the Earth's magnetotail and filled with hot, dense plasma and plays a crucial role in mass and energy transport in the whole magnetosphere (e.g., Baumjohann et al. 1989; Christon et al. 1989; Huang and Frank 1994; Baker et al. 1996; Wing and Newell 1998). Firstly, charged particles and the energy from the solar wind can be injected into the plasma sheet from magnetotail through nightside reconnection during substorms (Baker et al. 1996). Secondly, the injected particles in plasma sheet can be precipitated into the Earth's atmosphere and generate the diffuse aurora via pitch angle scattering induced by kinds of plasma waves such as electron cyclotron harmonic (ECH) waves and whistler-mode chorus (Thorne et al. 2010; Ni et al. 2011a, 2011b, 2014, 2016). Thirdly, the protons and electrons in the plasma sheet are generally regarded as an important source of the ring current particles, which can be trapped by the Earth's magnetic field (Daglis et al. 1999). The Earth's radiation belt energetic particles, especially for the relativistic electrons

Electronic supplementary material The online version of this article (https://doi.org/10.1007/s10509-020-03819-0) contains supplementary material, which is available to authorized users.

✉ Z. Zou
zouzy@hit.edu.cn

1 Institute of Space Science and Applied Technology, Harbin Institute of Technology Shenzhen, Shenzhen, China

2 Helmholtz Centre Potsdam, GFZ German Research Centre for Geosciences, Potsdam, Germany

3 Institute of Physics and Astronomy, University of Potsdam, Potsdam, Germany

4 Department of Space Physics, School of Electronic Information, Wuhan University, Wuhan, Hubei, China

Published online: 11 June 2020

(>1 MeV) or "killing electrons", have attracted scientific interests in recent decades due to their potential hazards to the astronomy activities by electrostatically discharging the surface of spacecraft instruments (e.g., Elkington et al. 2003; Shprits et al. 2005, 2008; Thorne et al. 2013). To help analyze and predicate the radiation belt (RB) dynamics, a large number of models have been made and progressed, such as (1) Fokker-Planck diffusion models (e.g., Albert and Bortnik 2009; Subbotin et al. 2011; Tu et al. 2013); (2) convection-diffusion models (e.g., Fok et al. 2008; Jordanova et al. 2016); (3) test particle simulations (e.g., Kress et al. 2007; Matsui et al. 2017); and (4) particle-in-cell codes and hybrid codes (e.g., Camporeale 2015). Recently, data assimilation models (Shprits et al. 2013, 2015; Aseev et al. 2019; Wang and Shprits 2019) and machine learning techniques (e.g., Koller et al. 2007; Ling et al. 2010) have also been used to the nowcast or forecast of RB dynamics. Among all the models above, one of the biggest challenges is to determine the outer spatial boundary conditions of electrons flux distributions, which are widely adopted from the central plasma sheet electrons. Since the limited operating orbits of the spacecraft, the electron fluxes at various energies cannot be directly measured in a continuously spatiotemporal space. Therefore, building up an accurate and reasonable model of the plasma sheet electron fluxes is an easy approach to setting up the outer boundary conditions for physics-based radiation belt simulations and further investigating the dynamics of other parts of the terrestrial magnetosphere.

Models of the variability of the plasma sheet plasma patterns have been constructed in recent years. Using solar wind and interplanetary magnetic field (IMF) indices as input, Tsyganenko and Mukai (2003) built an empirical model which can provide a two-dimensional spatial distribution of ion temperature (T_i), density (N_i), and pressure (P_i) in the central plasma sheet at radial distances from 10 to 50 R_E. Artemyev et al. (2013) studied the radial distribution of electron temperature in the magnetotail using THEMIS measurements at more than 10 R_E. Also utilizing THEMIS data at distance between 6 R_E and 11 R_E during the geomagnetic storm periods, Dubyagin et al. (2016) recently constructed an empirical model of the plasma sheet electron temperature dependence on solar wind indices. The correlation coefficients between the modeled results and the observations are 0.82 for the electron density and 0.76 for the electron temperature, indicating the good performance of the empirical models. It is noted that most of the previous empirical models have paid more attention to the characteristics of the ions or the temperature and density of the electrons, while the electron flux patterns have rarely been investigated yet. Also, since the limitations of the spacecraft measurements, these observation-based models could not fully reproduce the dynamics of the electron fluxes under various solar wind indices or geomagnetic conditions. Wang et al. (2011) have compared ion and electron flux distributions in the plasma sheet between the simulation results calculated from Rice Convection Model (RCM) with the statistical observations from THEMIS and Geotail data. There is a good agreement in outlines of the overall spatial distribution of the energy spectrum and energy fluxes of the electrons between the modeling results and the observations. However, since concentrating on the potential physical mechanisms of the convection of the particles, some statistic distributions of the electrons in this model would be ignored and hard to use for real event modeling by the wider scientific community. Besides, it has also been suggested that the energetic electrons in the central plasma sheet (CPS) region are highly correlated with hours' time lag of solar wind or geomagnetic disturbances (e.g., Burin des Roziers et al. 2009a, 2009b), while both the empirical and physical models in previous studies used the real-time value of these parameters as the model inputs.

In the present study, we adopt a new quantitative tool to predicate the spatial dynamics of plasma sheet electrons based on a three-hidden-layer Artificial Neural Network (ANN). Based on observations from THEMIS A, D, and E spacecraft from April 1, 2007 to December 30, 2015, the ANN model has been trained, validated, and tested with the time series of 8 geomagnetic and solar wind indices as inputs and the spatial locations of the spacecraft measurements. The comparison between the statistical observations and the model result shows that the present ANN model could accurately and quickly reproduce global electron fluxes of plasma sheet at different continues energies (0.06 - 293 keV) from radial distance 7 R_E to 12 R_E (where R_E is the Earth's radius) at the nightside between 18 MLT through 24 MLT and up to 0.6 MLT (Magnetic Local Time) for any given corresponding time series of geomagnetic and solar wind indices. It could be readily adopted for building up the boundary conditions for physics-based simulation efforts that model the dynamics of the radiation belt electrons and other parts of the terrestrial magnetosphere. In this paper, we will first describe the data we use and the criteria to select them in Sect. 2. Then we present the detailed construction and the performance of our ANN model in Sect. 3. Finally, we present discussions and a summary in Sect. 4.

2 Data and observations

2.1 Database

In the present study, we use electron flux observations of the THEMIS A, D, and E spacecraft (Angelopoulos 2008a) from April 1, 2007 to December 30, 2015. We combine 5-minute averaged data from the electrostatic analyzer (ESA) (McFadden et al. 2008) and the Solid State Tele-

scope (SST) (Angelopoulos 2008a). To investigate the electron fluxes in the central plasma sheet, we limit the data in magnetic local time (MLT) from 18 MLT through 24 MLT and up to 06 MLT as well as radial distance (r), from 7 R_E to 12 R_E. To make sure the data are measured in and near the Earth's equatorial plane, we only use the measurements that satisfy the following criteria:

(1) The measurements are selected when $\sqrt{Bx^2 + By^2} <$ 15 nT, where B_x and B_y mean the x- and y-components of the measured amplitude of background magnetic field in GSM coordinate.
(2) We only use measurements with the highest equatorial pitch angle higher than 80°. The equatorial pitch angles are obtained using the magnetic field model TS07D (Tsyganenko and Sitnov 2007).

we calculate the omnidirectional number flux by integrating differential flux in each pitch angle:

$$f_{omni} = 2[2\pi \int_0^{\frac{\pi}{2}} f(\alpha) \sin(\alpha)\, d\alpha] \quad (1)$$

where f_{omni} is the omnidirectional flux, α is equatorial pitch angle, and f is the differential flux at each pitch angle. The measurements, where less than 4 pitch angle channels are available, are also eliminated to make sure the accuracy of the integration. Henceforth, we refer to the omnidirectional number flux of the electrons as electron flux. We only use an intermediate range of electron energies, a total of 24 channels, from 0.06 keV to 293 keV. Finally, the whole database ('All dataset') is randomly divided as "training", "validation", and "test" sets with the ratio 6:2:2. In addition, 8 geomagnetic indices (AE, Dst; solar wind speed V_{sw}, dynamic pressure P_{dyn}, temperature T_{sw}, proton density N_p; the north component of the interplanetary magnetic field IMF-B_z, and the sunspot indicator F10.7) are also adopted from the Omni-web (ftp://spdf.gsfc.nasa.gov/pub/data/omni/high_res_omni) as the indicators of geomagnetic storms or substorms and solar wind activity. The number of the ESA and SST measurements from training combined with "validation set" and "test set" is shown in Fig. S1 in the Supporting Information.

2.2 Observations

Based on "training" combined with "validation" sets, Fig. 1 (a) and (b) show global distributions and energy spectrum of the plasma sheet electron fluxes (#/(s cm^2 keV)) during quiet, moderate, and active times, from 7 R_E to 12 R_E. Note that we only illustrate the flux distributions at 6 specialized energies (i.e. 0.3, 1.5, 7.7 31, 66 and 200 keV) in Fig. 1 (a). The distributions at the other 18 energy channels are shown in Fig. S2 in the Supporting Information. It is clear in Fig. 1 (a) that a pronounced MLT-asymmetry of electron fluxes appears at 0.3 keV to 31 keV, while it becomes less distinct as electron energy increases and disappears at 200 keV. This trend can also be found in Fig. 1 (b), where the electron fluxes at a few 0.1 keV to a few 10 keV in ∼1800 MLT (duskside) are much smaller than that in ∼0600 MLT (dawnside). Moreover, Fig. 1 (a) shows that the value of the electrons fluxes is significantly dependent on radial distances at lower energies (from 0.3 keV to 7.7 keV) but almost stays constant for that at higher energies (from 7.7 keV to 200 keV). Furthermore, the electron flux grows when activity intensifies, especially for the population at energies less than a few 10 keV at midnight and dawnside, as shown in both Fig. 1 (a) and Fig. 1 (b). The result above is consistent with the observation from Wang et al. (2011), in which they used the electron data based on the THEMIS and Geotail spacecraft and also found the dawn-dusk asymmetry and radial-distance dependence that are functions of energy. For plasma sheet electrons, the thermal energy increases from 1 keV at the tail to a few keV in the near-Earth region, with higher energy in post-midnight to dawn sectors than pre-midnight to dusk sectors (Wang et al. 2011). As activity intensifies, the electrons at energies from ∼ keV to ∼10 keV are injected from the magnetotail via magnetic reconnection to the plasma sheet midnight sector and then drift eastward which makes the electrons increase in energy in post-midnight and dawn sectors. When the electrons drift to the dayside, most of them will be lost to the magnetopause especially happens at larger L-shells, leading to much lower electron fluxes at dusk to post-midnight sectors. For electrons at higher energies (∼10 keV and ∼100 keV), the main population originates from the current ring to outer radiation belt, with a flux peak at from 4.5 R_E to 6 R_E or lower radial distances, showing a pronounced dependence on radial distance. Unlike the electrons that are injected or convected, there are almost symmetric with respect to different MLT sectors.

3 ANN model

3.1 Model construction

Here, we build an empirical model of plasma sheet electron fluxes by using Artificial Neural Network (ANN) method, which is considered as a generic and convenient approach to modeling complex, nonlinear functions, and have been widely used in magnetospheric studies (e.g. Bortnik et al. 2016; Chu et al. 2017a, 2017b; Kim et al. 2013; Souza et al. 2016; Zhelavskaya et al. 2016, 2017). The architecture of the ANN model is schematically shown in Fig. 2. It is composed of an input layer with 83 features, three hidden layers with 150, 100, and 50 neurons in the first, second, and third hidden layers, and a single output, logarithm of electron flux, $\log_{10}(f)$. The activation function here is selected

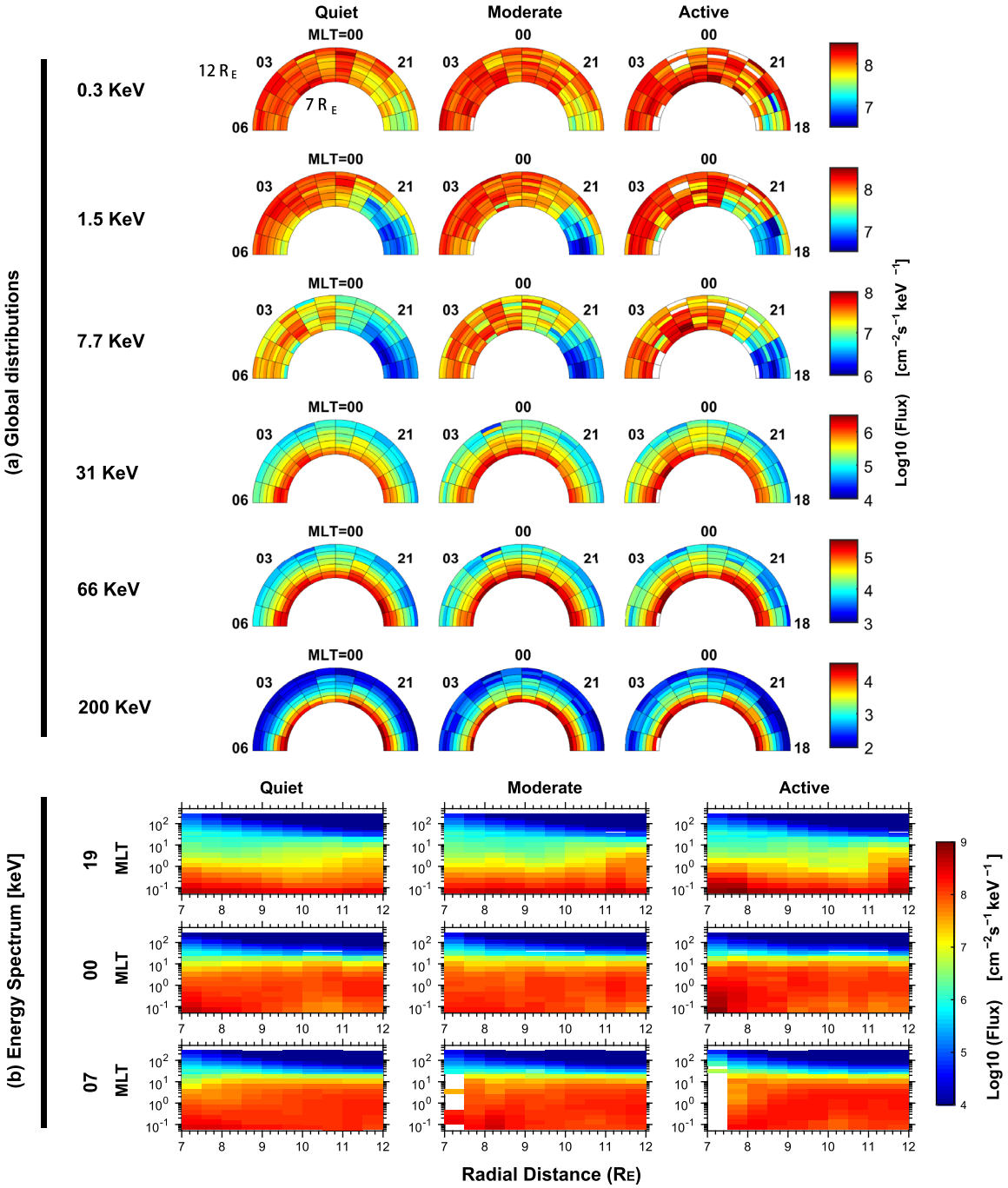

Fig. 1 (**a**) Global distribution of averaged plasma sheet electron omnidirectional number fluxes from Training and Validation dataset between the radial distance 7 R_E and 12 R_E from 1800 MLT to 0600 MLT, for 6 different energies in the quiet, moderate and active times. (**b**) Energy Spectrum of averaged plasma sheet electron omnidirectional number fluxes from Training and Validation dataset as a function of radial distance (r, unit: R_E) in each corresponding bin between 3 specialized MLT sectors at the quiet, moderate and active times. The width of the MLT sectors is 0.5 MLT

as a Rectified Linear Unit (the ReLU, (Glorot et al. 2011) nonlinear function (illustrated in the right bottom corners in Fig. 2) in each neuron of the hidden layers or a linear function in the output layer. With better performance in convergence than traditional (e.g., sigmoid function) activation function, the ReLU function is widely regarded as an appropriate one for neural network regressions (Chollet and Allaire 2018). Since the dynamics of electron flux evolution of plasma sheet electrons is highly dependent on a variety of geomagnetic and solar wind indices as well as its preced-

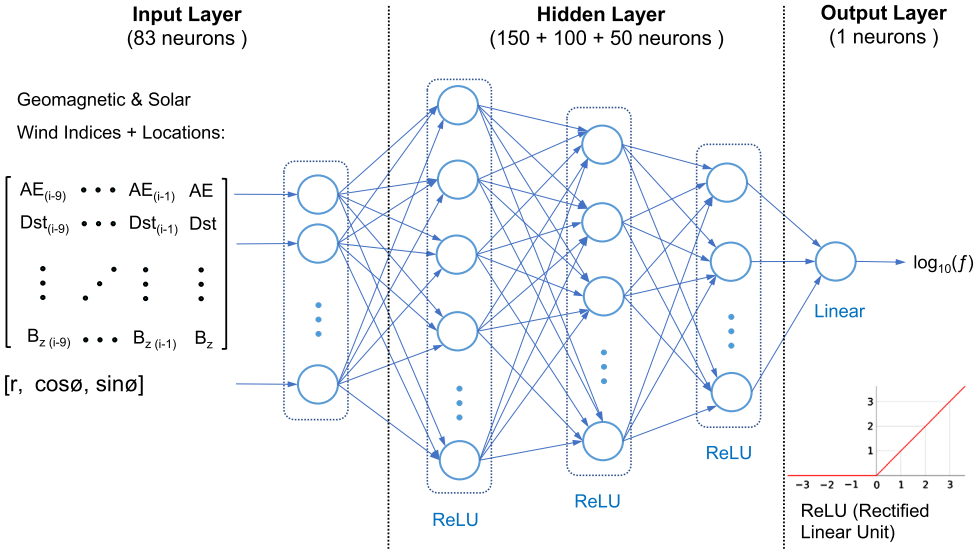

Fig. 2 Architecture of the artificial neural network model, with 150, 100, and 50 neurons in the first, second, and third hidden layers, respectively. The input parameters include the geomagnetic and solar wind indices as well as their history with 9 time-lags (1, 2, 3, 6, 12, 18, 24, 36, 48 hours), and the locations with r, cosø, and sinø. The target parameter is the logarithm of electron flux, $\log_{10}(f)$. The action functions in hidden and output layers are adopted as Rectified linear unit (ReLU) and linear functions, respectively

ing states, we adopt time series of these indices (8 indices, listed Sect. 2.1, and their time lags with 1, 2, 3, 6, 12, 18, 24, 36, 48 hours, a total of 80 parameters) and the locations of observations (r, cosø, and sinø, here ø represents the MLT angle (MLT/24 $\times 2\pi$), a total of 4 parameters) as inputs. To eliminate possible skewness in data that could happen due to a different range, the inputs have to be normalized to a range from 0 to 1 before training. The ANN model is trained using Scaled Conjugate Gradient (SCG) backpropagation to minimize the mean-square error (MSE) of the logarithm of the electron fluxes. The MSE of the test set, which is independent of the model construction, can be used as an indicator of its out-of-sample performance or the ability to predict. To avoid overfitting and improve the generalizability of our neural network model, 'early stopping' process is adopted in our model, which will stop the training process and save the current weights and biases of each neuron when the validation set stops improving for several consecutive steps. With the optimized ANN model available, we test it by comparison between the statistical observation from the test set, and the model reproduced values. The result is present in Sect. 3.2.

3.2 Model performance

Figure 3 shows the regression between the observations and predicted values of omnidirectional electron fluxes for 'All', 'Training', 'Validation', and 'Test' sets at 6 specified energies as in Fig. 1 (a) (the regression at other 18 energy channels are shown in Fig. S3 in the Supporting Information). The color shows the number of samples in each bin. The diagonal line, which represents a perfect agreement between the observations and modeled values, is also illustrated in each subplot. The correlation coefficient (R) and the root mean square error (RMSE) are also marked in each subplot as coefficients to judge the goodness of the ANN model. Overall, most of the points are centered along with the diagonal line in all data sets, indicating that our ANN model can accurately reproduce almost all observations. The correlation coefficient (R) at each 6 energy for 'All', 'Training' and 'Validation' sets are close and greater than 0.95, which means that the neural network can substantially explain $R^2 = \sim 90\%$ of the observed variability. Since the 'Test' data set is not used in the training process, the correlation coefficient (R) has an unignorable drop, especially at 0.3 keV with R $\sim$0.91 ($R^2 = \sim 83\%$). It is evident that our neural network has a good capability to predict out-of-sample distributions. The root-mean-square-error (RMSE) on the test data set of the logarithm of the electron fluxes is less than 0.36, which can be translated to a factor of $10^{0.36} = 2.29$. It suggests that the neural network model can predict out-of-sample observations around a factor of 2.29 error. Both the coefficients for judging the fitted goodness above demonstrate that our model can accurately reproduce the observations of plasma sheet electron fluxes and have a strong ability of predictions.

Figure 4 shows the comparison of the global distributions of the electron fluxes at 6 specified energies (the results at other 18 energy channels are shown in Fig. S4 in the Supporting Information) between the (a) observation from 'Test' set and (b) values reproduced by our ANN model during various substorm condition. The normalized difference (σ) between them is also illustrated in Fig. 4 (c). Here, $\sigma = 2|(f_{\mathrm{mod}} - f_{\mathrm{obs}})/(f_{\mathrm{mod}} + f_{obs})|$, where f_{obs} and f_{mod} are the logarithm of the observed and the modeled electron fluxes. Figure 5 shows the comparison between the observations and model results in the same format as Fig. 4 but for the energy spectrum versus L-shell, using all 24 measured energy channels from 0.06 keV to 293 keV. First, it is evident that the modeled result in both figures is in agreement with the observations including the order of the fluxes

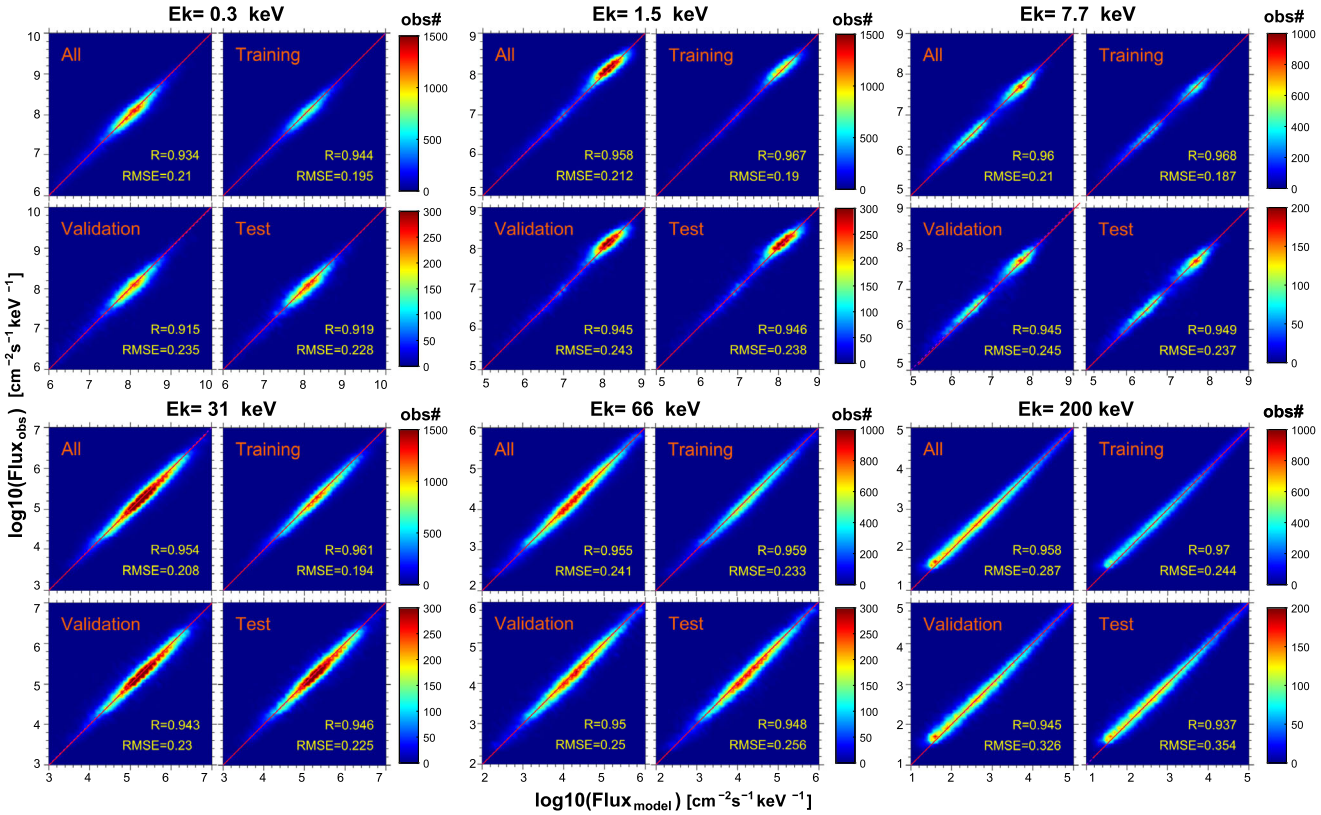

Fig. 3 Correlation between in situ observed logarithm of electron flux, $\log_{10}(f)$, and the modeled values by ANN model for the datasets (All, Training, Validation, and Test) for 6 specified energies. The bin size is 0.1 order for both observed and modeled values in each subplot, and the color indicates the number of observations in each bin. The red dashed lines are the diagonal indicating perfect agreement ($y = x$). The correlation coefficients (R) and root-mean-square-error (RMSE) are shown in the right bottom corners

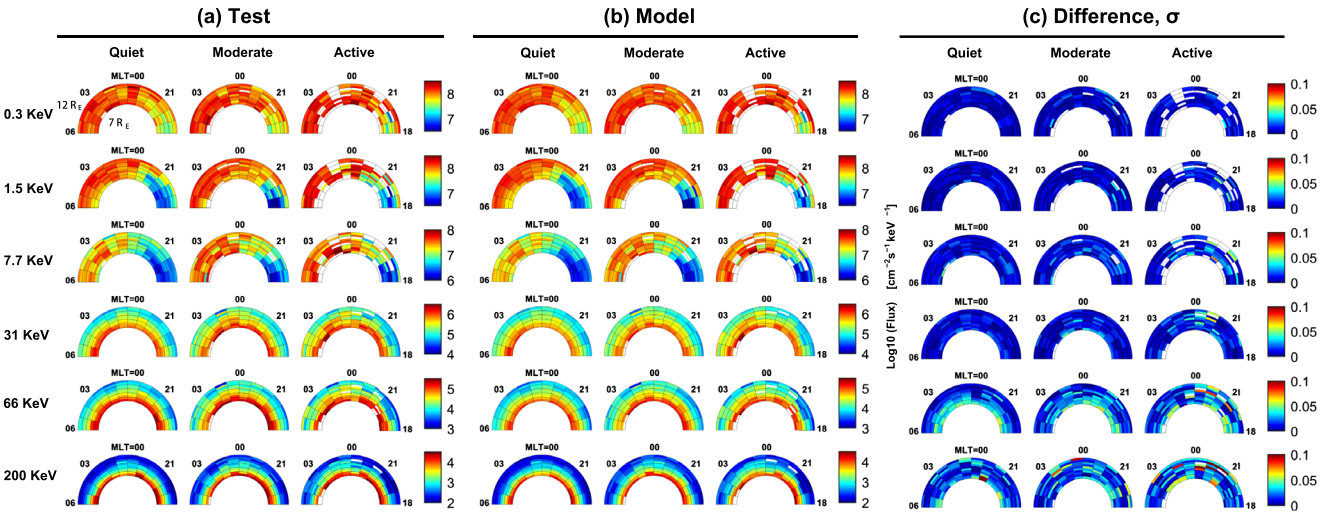

Fig. 4 The same format as Fig. 2 but for (**a**) observations from Test dataset, (**b**) the predicted result from the ANN model, and (**c**) the difference (σ) between them

at all energies and the total configuration of them in different spatial locations. Moreover, the dawn-dusk asymmetric distributions of the electron fluxes at energies less than 66 keV can also be clearly identified with a moderate change along with the MLT sectors, as well as the obvious dependence on radial distances of that at higher energies. The normalized difference (σ) are almost less than 0.05 in most of the spatial locations at all energies also indicating a small er-

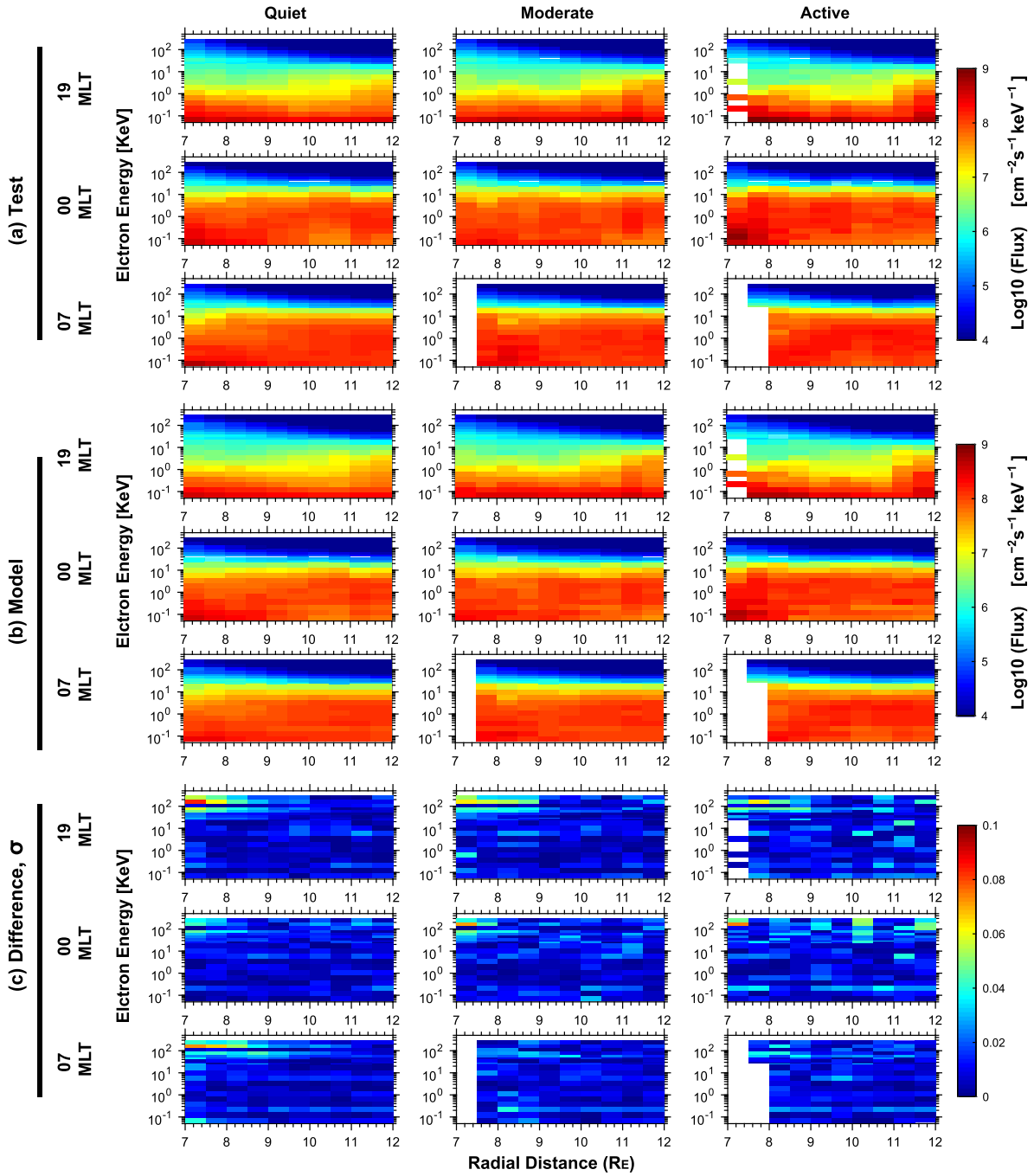

Fig. 5 The same format as Fig. 3 but for (**a**) observations from Test dataset, (**b**) the predicted result from the ANN model, and (**c**) the difference (σ) between them

ror between the modeled electron fluxes and the observations. As the energy increases, the normalized difference increases, especially at $r = 7 \sim 9$ R_E, in which σ is close to 0.1, as shown in the bottom row (200 keV) in Fig. 4c and quiet time error of $100 \sim 200$ keV in Fig. 5c. This can be found in Fig. 5, where the root-mean-square error (RMSE) for 'Test' set increases from 0.228 at Ek = 0.3 keV to 0.354 at Ek = 200 keV, our ANN model performs a little better at lower energies. One of the possible reasons could be that electrons at lower energies are more sensitive to the variation of solar wind/geomagnetic activity, while electrons at higher energies are also influenced by other indirect physical mechanisms. For instance, the electrons at ~100 keV can be originally accelerated via inward radial diffusion from substorm injected electrons at ~10 keV, thus showing a time delay or not so clear correlations to changes of the solar wind and geomagnetic indices as that for ~10 keV electrons. Overall, the very high consistency and low error be-

tween the modeled result and observations demonstrate the excellent capabilities of our neural network model in statistically reproducing the plasma sheet electron fluxes for various substorm activity.

4 Discussions and summary

In the present study, we used the data from ESA and SST detectors onboard the THEMIS – A/D/E spacecraft during the time period from April 1, 2007 to December 30, 2015 to statistically investigate the plasma sheet number electron fluxes at energies from 0.06 to 293 keV from 7 to 12 R_E on the nightside (18-06 MLT) under various geomagnetic activity conditions. With time series of geomagnetic/solar wind indices and locations of observations as inputs, as well as ReLU or linear function as active functions in each neuron, we constructed a three-hidden-layer, full connection ANN model. The model was trained using SCG backpropagation to minimize its MSE of the logarithm of the electron fluxes. We used an 'early stopping' process to avoid overfitting and improve the generalizability of our neural network model. Using this model, we check its performance using the Dataset 2, our 'Test' set.

Compared with previous empirical and physical models, our ANN model of the plasma sheet electron fluxes presents three advantages. First, The result of regression showed that almost all the observations can be accurately reproduced by the ANN model with total correlation coefficient (R) ~0.91 and RMSE less than 0.36, indicating that the model can substantially explain $R^2 =\sim 83\%$ of the observed variability and can predict out-of-sample observations around a factor of 2.29 error. Further investigation of the performance on global distributions and the energy spectrum indicates that our ANN model can accurately capture the total configuration of electron flux distributions in different spatial locations under various geomagnetic activity, with the normalized difference (σ) are close or less than 0.01. Also, the dawn-dusk asymmetry and dependence on radial distances can also be clearly identified by the model. With higher consistency and lower error compared to previous models, we conclude that our artificial neural network (ANN) has an excellent capability in statistically reproducing the plasma sheet electron fluxes for various activity levels. Second, since the spatiotemporal dynamics of plasma sheet electrons are highly sensitive to multiple solar wind and geomagnetic disturbances as well as their time lags, only considering the real-time values of one or two indices would be not enough to present the comprehensive and indirect influences of solar wind on the whole plasma sheet patterns. In the current ANN model, time series of these indices 8 indices their time lags have first been adopted as the inputs, which is believed to improve both the creditability and the ability of the model predictions. Third, previous physical models would consume a large number of CPU time (e.g., hours to months to obtain long time change of electron distributions) when operated, while the present ANN model can quickly provide high-resolution and reasonable results in spatiotemporally continue domains at a timescale of few seconds when given the inputs. Overall, it can be suggested that our ANN model could supply a convenient and more accurate way to quantitatively predicate the critical patterns in the central plasma sheet.

It is worthwhile to note that the current ANN model as well as other numeral predictive techniques, are not and could never be a substitute for physical modeling or understanding as suggested in recent reports (Anderson 2008), but can give further insight to the physics due to their spatial and temporal predictive ability. Given the time series of the 8 geomagnetic or solar wind indices, the ANN model can easily provide all the electron flues at 24 energies from 7 R_E to 12 R_E at all MLT sectors in the plasma sheet, which are not able to measure by spacecraft or ground-based instruments. This time-dependent global survey of plasma sheet electrons can help convert sparse spacecraft observations, thus validating the physical models of plasma sheet and other parts in the Earth's magnetosphere, such as the evolutional model of the radiation belt electron fluxes.

The conclusion can be summarized as follows.

(1) A three hidden-layer Artificial Neural Network has first been constructed with time series of 8 solar wind/geomagnetic indices as inputs, which provides a new and feasible approach to predicate the distributions of electron fluxes in the central plasma sheet.
(2) Compared with previous empirical and physical models, the current ANN model can give more accurate (total correlation coefficient above ~0.91 and a root-mean-square-error less than 0.36) and spatiotemporally continue predictions in high resolutions within less time (a few seconds).
(3) The ANN model can be readily adopted for building up the boundary conditions for physics-based simulation efforts that model the dynamics of the radiation belt electrons and other parts of the terrestrial magnetosphere.

Acknowledgements We would also like to thank Alexander Drozdov and Adam Kellerman for useful discussions. This work was supported by the NSFC grants 4173000045, 41674163, 41474141, and the Hubei Province Natural Science Excellent Youth Foundation (2016CFA044). This research has been partially funded by Deutsche Forschungsgemeinschaft through grant CRC 1294 "Data Assimilation", Project B06 "Novel methods for the 3D reconstruction of the dynamic evolution of the Van Allen belts using multiple satellite measurements". The ESA and SST data are obtained from https://spdf.gsfc.nasa.gov/pub/data/themis. The data of geomagnetic indices are available from the NASA OmniWeb (http://cdaweb.gsfc.nasa.gov). The ANN models are available in https://github.com/ZhengyangZou/ANN-model-for-CPS.

References

Albert, J.M., Bortnik, J.: Nonlinear interaction of radiation belt electrons with electromagnetic ion cyclotron waves. Geophys. Res. Lett. **36**, L12110 (2009). https://doi.org/10.1029/2009GL038904

Anderson, C.: The end of theory: the data deluge makes the scientific method obsolete, Wired, June 23, 2008. Available at http://www.wired.com/science/discoveries/magazine/16-07/pb_theory

Angelopoulos, V.: The THEMIS mission. Space Sci. Rev. **141**, 5–34 (2008a). https://doi.org/10.1007/s11214-008-9336-1

Angelopoulos, V.: First results from the THEMIS mission. Space Sci. Rev. **141**, 453–476 (2008b)

Artemyev, A.V., Petrukovich, A.A., Nakamura, R., Zelenyi, L.M.: Profiles of electron temperature and B_z along Earth's magnetotail. Ann. Geophys. **31**, 1109–1114 (2013). https://doi.org/10.5194/angeo-31-1109-2013

Aseev, N.A., Shprits, Y.Y., Wang, D., Wygant, J., Drozdov, A.Y., Kellerman, A.C., Reeves, G.D.: Transport and loss of ring current electrons inside geosynchronous orbit during the 17 March 2013 storm. J. Geophys. Res. Space Phys. **124**, 915–933 (2019). https://doi.org/10.1029/2018JA026031

Baker, D.N., Pulkkinen, T.I., Angelopoulos, V., Baumjohann, W., McPherron, R.L.: Neutral line model of substorms: past results and present view. J. Geophys. Res. **101**, 12,975 (1996). https://doi.org/10.1029/95JA03753

Baumjohann, W., Paschmann, G., Cattell, C.A.: Average plasma properties in the central plasma sheet. J. Geophys. Res. **94**, 6597 (1989). https://doi.org/10.1029/JA094iA06p06597

Bortnik, J., Li, W., Thorne, R.M., Angelopoulos, V.: A unified approach to inner magnetospheric state prediction. J. Geophys. Res. Space Phys. **121**, 2423–2430 (2016). https://doi.org/10.1002/2015JA021733

Burin des Roziers, E., Li, X., Baker, D.N., Fritz, T.A., Friedel, R., Onsager, T.G., Dandouras, I.: Energetic plasma sheet electrons and their relationship with the solar wind: a cluster and geotail study. J. Geophys. Res. **114**, A02220 (2009a). https://doi.org/10.1029/2008JA013696

Burin des Roziers, E., Li, X., Baker, D.N., Fritz, T.A., McPherron, R.L., Dandouras, I.: Cluster observations of energetic electron flux variations within the plasma sheet. J. Geophys. Res. **114**, A11208 (2009b). https://doi.org/10.1029/2009JA014239

Camporeale, E.: Resonant and nonresonant whistlers-particle interaction in the radiation belts. Geophys. Res. Lett. **42**, 3114–3121 (2015). https://doi.org/10.1002/2015GL063874

Chollet, F., Allaire, J.J.: Deep learning with R. Shelter Island: Manning Publications Co. Biometrics **76**, 361–362 (2018)

Christon, S.P., Williams, D.J., Mitchell, D.G., Frank, L.A., Huang, C.Y.: Spectral characteristics of plasma sheet ion and electron populations during undisturbed geomagnetic conditions. J. Geophys. Res. **94**, 13,409–13,424 (1989)

Chu, X.N., Bortnik, J., Li, W., Ma, Q., Angelopoulos, V., Thorne, R.M.: Erosion and refilling of the plasmasphere during a geomagnetic storm modeled by a neural network. J. Geophys. Res. Space Phys. **122**, 7118–7129 (2017a). https://doi.org/10.1002/2017JA023948

Chu, X., et al.: A neural network model of three-dimensional dynamic electron density in the inner magnetosphere. J. Geophys. Res. Space Phys. **122**, 9183–9197 (2017b). https://doi.org/10.1002/2017JA024464

Daglis, I.A., Thorne, R.M., Baumjohann, W., Orsini, S.: The terrestrial ring current: origin, formation, and decay. Rev. Geophys. **37**, 407–438 (1999). https://doi.org/10.1029/1999RG900009

Dubyagin, S., Ganushkina, N.Y., Sillanp, I., Runov, A.: Solar wind-driven variations of electron plasma sheet densities and temperatures beyond geostationary orbit during storm times. J. Geophys. Res. Space Phys. **121**, 8343–8360 (2016). https://doi.org/10.1002/2016JA022947

Elkington, S.R., Hudson, M.K., Chan, A.A.: Resonant acceleration and diffusion of outer zone electrons in an asymmetric geomagnetic field. J. Geophys. Res. **108**(A3), 1116 (2003). https://doi.org/10.1029/2001JA009202

Fok, M.-C., Horne, R.B., Meredith, N.P., Glauert, S.A.: Radiation belt environment model: application to space weather nowcasting. J. Geophys. Res. **113**, A03S08 (2008). https://doi.org/10.1029/2007JA012558

Glorot, X., Bordes, A., Bengio, Y.: Deep sparse rectifier neural networks. In: Gordon, I., Dunson, D., Dudík, M. (eds.) Proceedings of the Fourteenth International Conference on Artificial Intelligence and Statistics, vol. 15, pp. 315–323 (2011). Fort Lauderdale, FL: PMLR. Retrieved from. http://proceedings.mlr.press/v15/glorot11a.html

Huang, C.Y., Frank, L.A.: A statistical survey of the central plasma sheet. J. Geophys. Res. **99**, 83 (1994). https://doi.org/10.1029/97JA01894

Jordanova, V.K., Tu, W., Chen, Y., Morley, S.K., Panaitescu, A.-D., Reeves, G.D., Kletzing, C.A.: RAM-SCB simulations of electron transport and plasma wave scattering during the October 2012 "double-dip" storm. J. Geophys. Res. Space Phys. **121**, 8712–8727 (2016). https://doi.org/10.1002/2016JA022470

Kim, K.-C., Shprits, Y., Lee, J., Hwang, J.: Empirically modeled global distribution of magnetospheric chorus amplitude using an artificial neural network. J. Geophys. Res. Space Phys. **118**, 6243–6253 (2013). https://doi.org/10.1002/jgra.50595

Koller, J., Chen, Y., Reeves, G.D., Friedel, R.H.W., Cayton, T.E., Vrugt, J.A.: Identifying the radiation belt source region by data assimilation. J. Geophys. Res. **112**, A06244 (2007). https://doi.org/10.1029/2006JA012196

Kress, B.T., Hudson, M.K., Looper, M.D., Albert, J., Lyon, J.G., Goodrich, C.C.: Global MHD test particle simulations of >10 MeV radiation belt electrons during storm sudden commencement. J. Geophys. Res. **112**, A09215 (2007). https://doi.org/10.1029/2006JA012218

Ling, A.G., Ginet, G.P., Hilmer, R.V., Perry, K.L.: A neural network-based geosynchronous relativistic electron flux forecasting model. Space Weather **8**, S09003 (2010). https://doi.org/10.1029/2010SW000576

Matsui, H., Torbert, R.B., Spence, H.E., Argall, M.R., Alm, L., Farrugia, C.J., et al.: Relativistic electron increase during chorus wave activities on the 6–8 March 2016 geomagnetic storm. J. Geophys. Res. Space Phys. **122**, 11,302–11,319 (2017). https://doi.org/10.1002/2017JA024540

McFadden, J.P., Carlson, C.W., Larson, D., Angelopolos, V., Ludlam, M., Abiad, R., Elliot, B.: The THEMIS ESA plasma instrument and in-flight calibration. Space Sci. Rev. **141**, 277–302 (2008)

Ni, B., Thorne, R.M., Horne, R.B., Meredith, N.P., Shprits, Y.Y., Chen, L., Li, W.: Resonant scattering of plasma sheet electrons leading to diffuse auroral precipitation: 1. Evaluation for electrostatic electron cyclotron harmonic waves. J. Geophys. Res. **116**, A04218 (2011a). https://doi.org/10.1029/2010JA016232

Ni, B., Thorne, R.M., Meredith, N.P., Horne, R.B., Shprits, Y.Y.: Resonant scattering of plasma sheet electrons leading to diffuse auroral precipitation: 2. Evaluation for whistler mode chorus waves. J. Geophys. Res. **116**, A04219 (2011b). https://doi.org/10.1029/2010JA016233

Ni, B., Bortnik, J., Nishimura, Y., Thorne, R.M., Li, W., Angelopoulos, V., Ebihara, Y., Weatherwax, A.T.: Chorus wave scattering responsible for the Earth's dayside diffuse auroral precipitation:

a detailed case study. J. Geophys. Res. Space Phys. **119**, 897–908 (2014). https://doi.org/10.1002/2013JA019507

Ni, B., Thorne, R.M., Zhang, X., Bortnik, J., Pu, Z., Xie, L., Hu, Z.-J., Han, D., Shi, R., Zhou, C., Gu, X.: Origins of the Earth's diffuse auroral precipitation. Space Sci. Rev. **200(1)**, 205–259 (2016). https://doi.org/10.1007/s11214-016-0234-7

Shprits, Y.Y., Thorne, R.M., Reeves, G.D., Friedel, R.: Radial diffusion modeling with empirical lifetimes: comparison with CRRES observations. Ann. Geophys. **23**(4), 1467–1471 (2005). https://doi.org/10.5194/angeo-23-1467-2005

Shprits, Y.Y., Subbotin, D.A., Meredith, N.P., Elkington, S.R.: Review of modeling of losses and sources of relativistic electrons in the outer radiation belts: II. Local acceleration and loss. J. Atmos. Sol.-Terr. Phys. **70**(14), 1694–1713 (2008). https://doi.org/10.1016/j.jastp.2008.06.014

Shprits, Y., Kellerman, A., Kondarashov, D., Subbotin, D.: Application of a new data operator-splitting data assimilation technique to the 3-D VERB diffusion code and CRRES measurements. Geophys. Res. Lett. **40**, 4998–5002 (2013). https://doi.org/10.1002/grl.50969

Shprits, Y.Y., Kellerman, A.C., Drozdov, A.Y., Spence, H.E., Reeves, G.D., Baker, D.N.: Combined convective and diffusive simulations: VERB-4D comparison with 17 March 2013 Van Allen probes observations. Geophys. Res. Lett. **42**, 9600–9608 (2015). https://doi.org/10.1002/2015GL065230

Souza, V.M., et al.: A neural network approach for identifying particle pitch angle distributions in Van Allen Probes data. Space Weather **14**, 275–284 (2016). https://doi.org/10.1002/2015SW001349

Subbotin, D.A., Shprits, Y.Y., Ni, B.: Long-term radiation belt simulation with the VERB 3-D code: comparison with CRRES observations. J. Geophys. Res. **116**, A12210 (2011). https://doi.org/10.1029/2011JA017019

Thorne, R.M., et al.: Scattering by chorus waves as the dominant cause of diffuse auroral precipitation. Nature **467**, 943–946 (2010). https://doi.org/10.1038/nature09467

Thorne, R.M., et al.: Rapid local acceleration of relativistic radiation belt electrons by magnetospheric chorus. Nature **504**, 411–414 (2013). https://doi.org/10.1038/nature12889

Tsyganenko, N.A., Mukai, T.: Tail plasma sheet models derived from geotail particle data. J. Geophys. Res. **108**(A3), 1136 (2003). https://doi.org/10.1029/2002JA009707. 2003

Tsyganenko, N.A., Sitnov, M.I.: Magnetospheric configurations from a high-resolution data-based magnetic field model. J. Geophys. Res. **112**, A06225 (2007)

Tu, W., Cunningham, G.S., Chen, Y., Henderson, M.G., Camporeale, E., Reeves, G.D.: Modeling radiation belt electron dynamics during GEM challenge intervals with the DREAM3D diffusion model. J. Geophys. Res. Space Phys. **118**, 6197–6211 (2013). https://doi.org/10.1002/jgra.50560

Wang, D., Shprits, Y.Y.: On how high-latitude chorus waves tip the balance between acceleration and loss of relativistic electrons. Geophys. Res. Lett. **46**, 7945–7954 (2019). https://doi.org/10.1029/2019GL082681

Wang, C.-P., Gkioulidou, M., Lyons, L.R., Wolf, R.A., Angelopoulos, V., Nagai, T., Weygand, J.M., Lui, A.T.Y.: Spatial distributions of ions and electrons from the plasma sheet to the inner magnetosphere: comparisons between THEMIS-geotail statistical results and the Rice convection model. J. Geophys. Res. **116**, A11216 (2011). https://doi.org/10.1029/2011JA016809

Wing, S., Newell, P.T.: Central plasma sheet ion properties as inferred from ionospheric observations. J. Geophys. Res. **103**, 6785–6800 (1998). https://doi.org/10.1029/97JA02994

Zhelavskaya, I., Spasojevic, M., Shprits, Y., Kurth, W.: Automated determination of electron density from electric field measurements on the Van Allen Probes spacecraft. J. Geophys. Res. Space Phys. **121**, 4611–4625 (2016). https://doi.org/10.1002/2015JA022132

Zhelavskaya, I.S., Shprits, Y.Y., Spasojevic, M.: Empirical modeling of the plasmasphere dynamics using neural networks. J. Geophys. Res. Space Phys. **122**, 11,227–11,244 (2017). https://doi.org/10.1002/2017JA024406